Geochemistry Geophysics Geosystems G3
AN ELECTRONIC JOURNAL OF THE EARTH SCIENCES
Published by AGU and the Geochemical Society

Article
Volume 10, Number 8
20 August 2009
Q08014, doi:10.1029/2009GC002576
ISSN: 1525-2027

Using S wave receiver functions to estimate crustal structure beneath ice sheets: An application to the Transantarctic Mountains and East Antarctic craton

Samantha E. Hansen, Jordi Julià, and Andrew A. Nyblade
Department of Geosciences, Pennsylvania State University, University Park, Pennsylvania 16802, USA (shansen@geosc.psu.edu; jjulia@geosc.psu.edu; andy@geosc.psu.edu)

Moira L. Pyle and Douglas A. Wiens
Department of Earth and Planetary Sciences, Washington University, Saint Louis, Missouri 63130, USA (mpyle@artsci.wustl.edu; doug@wustl.edu)

Sridhar Anandakrishnan
Department of Geosciences, Pennsylvania State University, University Park, Pennsylvania 16802, USA (sak@essc.psu.edu)

[1] For seismic stations deployed on ice sheets, determining crustal structure using P wave receiver functions can be difficult since ice reverberations may mask P-to-S (Ps) conversions from the crust-mantle boundary (Moho). In this study, we assess the usefulness of S wave receiver functions (SRFs), which are not affected by ice multiples, for investigating crustal structure beneath ice sheets by analyzing broadband seismic data recorded across the Transantarctic Mountains (TAMs) and the East Antarctic (EA) craton. Clear S-to-P (Sp) conversions from the Moho are obtained using standard SRF processing methods and are easier to interpret than the corresponding Ps conversion on PRFs. When the Sp-S times are modeled together with 16–20 s Rayleigh wave group velocities, we obtain Moho depth estimates of ~40–45 km for the EA craton, consistent with average Precambrian crustal thickness found globally but ~9 km thicker than previously reported estimates. A somewhat thinner crust (~35–40 km) is obtained beneath the TAMs, suggesting that crustal buoyancy is at most a minor contributor to the uplift of the mountain range in this region.

Components: 5768 words, 5 figures.

Keywords: S wave receiver functions; ice sheets; Antarctica; Transantarctic Mountains.

Index Terms: 0902 Exploration Geophysics: Computational methods: seismic; 9310 Geographic Location: Antarctica (4207); 8103 Tectonophysics: Continental cratons.

Received 21 April 2009; **Revised** 22 June 2009; **Accepted** 9 July 2009; **Published** 20 August 2009.

Hansen, S. E., J. Julià, A. A. Nyblade, M. L. Pyle, D. A. Wiens, and S. Anandakrishnan (2009), Using S wave receiver functions to estimate crustal structure beneath ice sheets: An application to the Transantarctic Mountains and East Antarctic craton, *Geochem. Geophys. Geosyst.*, *10*, Q08014, doi:10.1029/2009GC002576.

1. Introduction

[2] S wave receiver functions (SRFs) are becoming a common technique to investigate seismic discontinuities within and below the lithosphere that cannot be well imaged using P wave receiver functions (PRFs). For example, it is well documented that multiples from P-to-S (Ps) conversions originating

at the crust-mantle boundary (Moho) on PRFs can mask Ps conversions from the lithosphere-asthenosphere boundary (LAB), making the lithospheric structure difficult to discern [e.g., *Farra and Vinnik*, 2000; *Wilson et al.*, 2006; *Yuan et al.*, 2006]. On SRFs, however, S-to-P (Sp) conversions from the LAB can be more easily identified because they arrive earlier than the direct S phase while all crustal multiples arrive later. Consequently, SRF studies of lithospheric thickness in many tectonic regions have been published over the past decade [e.g., *Farra and Vinnik*, 2000; *Li et al.*, 2004; *Kumar et al.*, 2005; *Hansen et al.*, 2007, 2009].

[3] A similar situation arises for seismic stations on ice sheets and glaciers. Multiples from the Ps conversion at the ice-rock interface may interfere with the Ps conversion from the Moho, making it more difficult to use PRFs from stations on ice to determine crustal thickness as compared to stations situated on rock [*Zelt and Ellis*, 1999; *Julià et al.*, 2004]. In this study, we use broadband seismic data recorded across the Transantarctic Mountains (TAMs) and the East Antarctic (EA) craton to ascertain the usefulness of SRFs for imaging the Moho beneath seismic stations deployed on ice (referred to hereafter as "ice stations"). An investigation of the lithospheric thickness beneath Antarctic stations using SRFs is ongoing. Our results indicate that Sp conversions from the Moho can be clearly identified on ice station SRFs. Moreover, when combined with Rayleigh wave group velocity measurements obtained from noise correlation [*Pyle et al.*, 2008], estimates of crustal thickness with an uncertainty of ±3 km can be obtained. For the Antarctic stations, our analysis yields crustal thickness estimates of ~40–45 km beneath EA, typical of Precambrian crustal thickness found globally, and somewhat thinner crust (~35–40 km) beneath the TAMs.

[4] In this paper, we first provide a review of the SRF technique and describe the Antarctic data set. Then, we outline our procedure using a simple grid search modeling approach to combine the SRF data with Rayleigh wave group velocities to estimate crustal thickness. Finally, we conclude by assessing the utility of the SRFs for estimating crustal structure beneath ice stations and discuss the tectonic implications of our results by comparing them to estimates of crustal thickness obtained from PRFs.

2. Data and Methodology

2.1. SRF Technique

[5] Details of the SRF technique have been described in several papers [e.g., *Kumar et al.*, 2005; *Hansen et al.*, 2007, 2009] but will briefly be reviewed here. To generate the SRFs, we select S waves with high signal-to-noise ratios from earthquakes with magnitudes larger than 5.7, depths less than 200 km, and distances between 60° and 80°. This range of depths and distances minimizes any potentially interfering teleseismic phases [*Wilson et al.*, 2006]. Recorded waveforms are first rotated from the north-east-vertical (N-E-Z) to the radial-transverse-vertical (R-T-Z) coordinate system using the event's back azimuth and are visually inspected to pick the S wave onset. The three-component records are then cut to focus on the section of the waveform that is 100 s prior to and 12 s after the S arrival. In most SRF studies, it is common practice to rotate the data a second time around the incidence angle into the SH-SV-P coordinate system. Since these studies tend to focus on imaging the LAB, which produces a fairly weak Sp conversion compared to that generated by the Moho, this second rotation helps to enhance the LAB conversion of interest [e.g., *Li et al.*, 2004; *Kumar et al.*, 2005; *Hansen et al.*, 2007, 2009]. However, since we are focused on imaging the more pronounced Moho conversion, this second rotation is not necessary. Using *Ligorria and Ammon*'s [1999] iterative time domain method, SRFs are generated by deconvolving the R component from the corresponding Z component, and both the time axes and the amplitudes of the SRFs are reversed to make the SRFs comparable to the more common PRFs [e.g., *Li et al.*, 2004; *Kumar et al.*, 2005]. The frequency content of the receiver function is controlled by the width factor of the Gaussian filter, a [*Ligorria and Ammon*, 1999]. Several values of a were examined; however, the best and most consistent results are obtained using an a of 1.0. To improve the signal-to-noise ratio, individual SRFs were stacked at each station.

2.2. SRFs for Antarctic Stations

[6] This study utilizes data from the Transantarctic Mountains Seismic Experiment (TAMSEIS), which operated from December 2000 to December 2003. The experiment included 41 temporary broadband stations distributed along the Antarctic coast, Ross Island, the TAMs, and into EA (Figure 1). The goals of TAMSEIS were to study the structure of the Precambrian EA craton as well as the origin of the TAMs. The TAMs are the largest noncollisional mountain range in the world [*ten Brink et al.*, 1997] and mark the boundary between the EA craton and Cenozoic, tectonically active West Antarctica (WA, Figure 1).

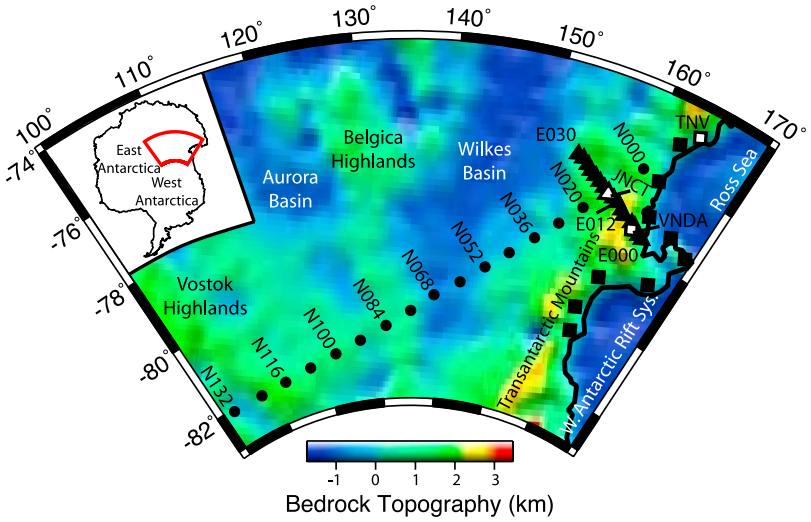

Figure 1. Map of the TAMSEIS seismic stations overlain on shaded relief bedrock topography from BEDMAP [*Lythe et al.*, 2001]. Stations along the EW and NS profiles are shown by black triangles and circles, respectively, except for station JNCT (white triangle), which is common to both profiles. Other TAMSEIS stations are shown by black squares. Two stations from the Global Seismograph Network, TNV and VNDA, are also shown for reference (white squares).

[7] Our study focuses on two main subarrays of the TAMSEIS network. The first subarray included 16 stations, spaced ~20 km apart, spanning a 300-km-wide region that strikes roughly east-west across the TAMs (EW profile, Figure 1). The second subarray included 17 stations, spaced ~80 km apart, which extended 1400 km from Terra Nova (TNV) NNE-SSW across the TAMs and onto the EA craton (NS profile, Figure 1). Since our primary goal is to evaluate SRFs for imaging the Moho beneath a substantial ice layer, we focused on stations located on the EA Ice Sheet. This included stations E012 through E030 along the EW profile and stations JNCT through N132 along the NS profile. However, to check the consistency of our results with those from previous PRF studies, we also computed SRFs for several stations deployed on rock ("rock stations") within the TAMs.

[8] Stacked SRFs for ice stations along both the EW and NS TAMSEIS profiles are shown in Figure 2. Some stations did not record enough useable data to generate a stack with a high signal-to-noise ratio, and these stations are not shown. Stacked SRFs were also generated for rock stations E004, E008,

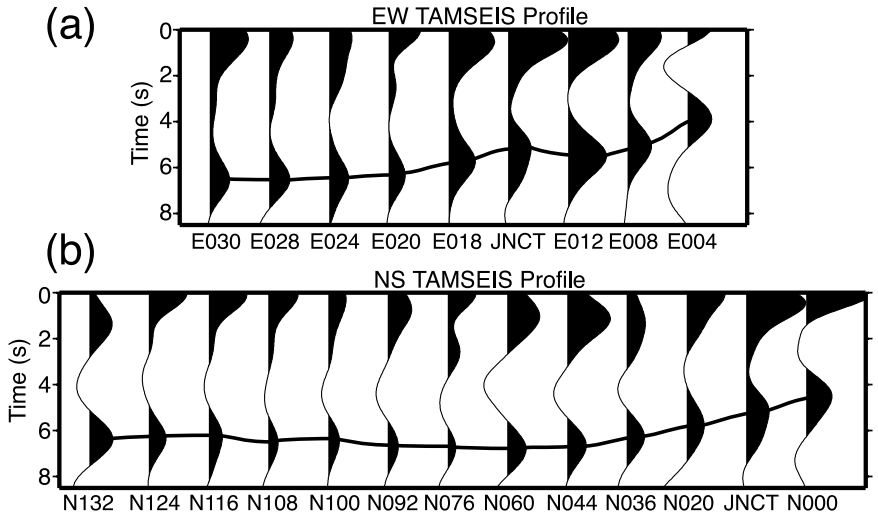

Figure 2. Stacked SRFs along the (a) EW and (b) NS TAMSEIS profiles. Stations E004, E008, and N000 are rock stations within the TAMs, and the rest are ice stations in EA. The black line denotes the Moho conversion from each station.

and N000 (Figure 2) for comparison to previous PRF studies. Since the SRFs have not been fully rotated to the SH-SV-P coordinate system, an initial arrival near 0 s is observed at all stations. For rock stations, this phase is the direct S arrival. However, for ice stations, this phase is the direct S arrival combined with the Sp conversion from the base of the ice. The *a* value of 1.0 used in our analysis produces a fairly wide filter that smears the two signals together. A second arrival is observed at all stations at approximately the expected time for an Sp conversion coming from the Moho. The timing of this conversion ranges between 3.9 and 6.6 s on the EW profile and between 4.5 and 6.8 s on the NS profile (Figure 2), where the variability of the timing indicates variations in crustal thickness or velocity.

2.3. Estimating Crustal Thickness

[9] To determine if the Sp times from the second arrival on the SRFs can be reasonably interpreted as the conversion from the Moho, we model the Sp-S arrival time along with Rayleigh wave group velocities to estimate Moho depth. Both the SRFs and dispersion data are sensitive to the same parameter, S wave velocity (V_s), but their corresponding constraints complement in such a way that they help bridge resolution gaps between the data sets [e.g., *Last et al.*, 1997]. The SRFs primarily constrain the vertical traveltime between the Moho and the surface while the dispersion data primarily constrain the average crustal V_s.

[10] Dispersion data for each TAMSEIS station were obtained from *Pyle et al.* [2008], who imaged the crust and upper mantle structure of the TAMs and surrounding areas using Rayleigh wave group velocities obtained from the cross correlation of ambient seismic noise. Their group velocity maps, which were obtained by tomographically inverting travel times between station pairs at periods between 5 and 23 s, are composed of equally spaced hexagonal blocks whose centers are 0.5° apart. To produce a smoothed group velocity dispersion curve, we averaged the group velocities within the block closest to each TAMSEIS station with those from the nearest surrounding blocks at each period. Along the EW TAMSEIS profile, the block spacing is wider than the station spacing, so the dispersion curves for some stations are the same (see Figure S1).[1] From the range of available periods most sensitive to crustal structure, we considered group velocities between 16 and 20 s because the number of paths used in the ambient noise tomography is reduced at longer periods, making these velocities somewhat less robust [*Pyle et al.*, 2008].

[11] Following the approach of *Last et al.* [1997], a grid search procedure was used to model the dispersion and SRF data. First, using subroutines from the DISPER80 package [*Saito*, 1988], synthetic dispersion curves were generated for various velocity-depth models and were compared to the observed group velocities. For the ice stations, the velocity-depth models consisted of four layers: an ice layer, a two-layer crust, and an upper mantle half-space. For each station, the thickness of the ice layer was determined by averaging ice thickness measurements acquired by ice-penetrating radar within several kilometers of the station [*Blankenship et al.*, 2001; *Studinger et al.*, 2004], and this thickness was fixed in the grid search (see Table S1). The V_s of both the ice layer and the uppermost mantle were also fixed at 1.8 and 4.5 km/s, respectively. Moho depth was allowed to vary between 25 and 52 km in 1 km increments, and the crust was parameterized as two layers of equal thickness. The velocities in each crustal layer were averaged by slowness to equal a nominal mean crustal shear velocity ($\overline{V}_s$), which was varied between 3.4 and 3.9 km/s. In all models, the Poisson's ratio (σ) of the ice, crust, and upper mantle were set to 0.33, 0.25, and 0.28, respectively. We used the same approach for the rock stations, except no ice layer was included in the corresponding velocity-depth models.

[12] Uncertainties associated with group velocity measurements obtained from ambient noise tomography depend on seasonal variability and generally increase with increasing period [e.g., *Yang et al.*, 2007]. Since no formal uncertainties were provided by *Pyle et al.* [2008], we conservatively examined the range of models whose predicted dispersion curves were within 0.05 and within 0.10 km/s of the observed group velocity data. While reducing our a priori uncertainty associated with the group velocity measurements reduced the number of "fit" models, there was little affect on the resulting mean Moho depth and $\overline{V}_s$ obtained.

[13] For each station, the models that fit the associated dispersion data within error were examined further by comparing their predicted Moho Sp time to the observed Moho Sp time on the corresponding stacked SRF. The depth and distance of each event contributing to the stack at a given station were

[1] Auxiliary materials are available in the HTML. doi:10.1029/2009GC002576.

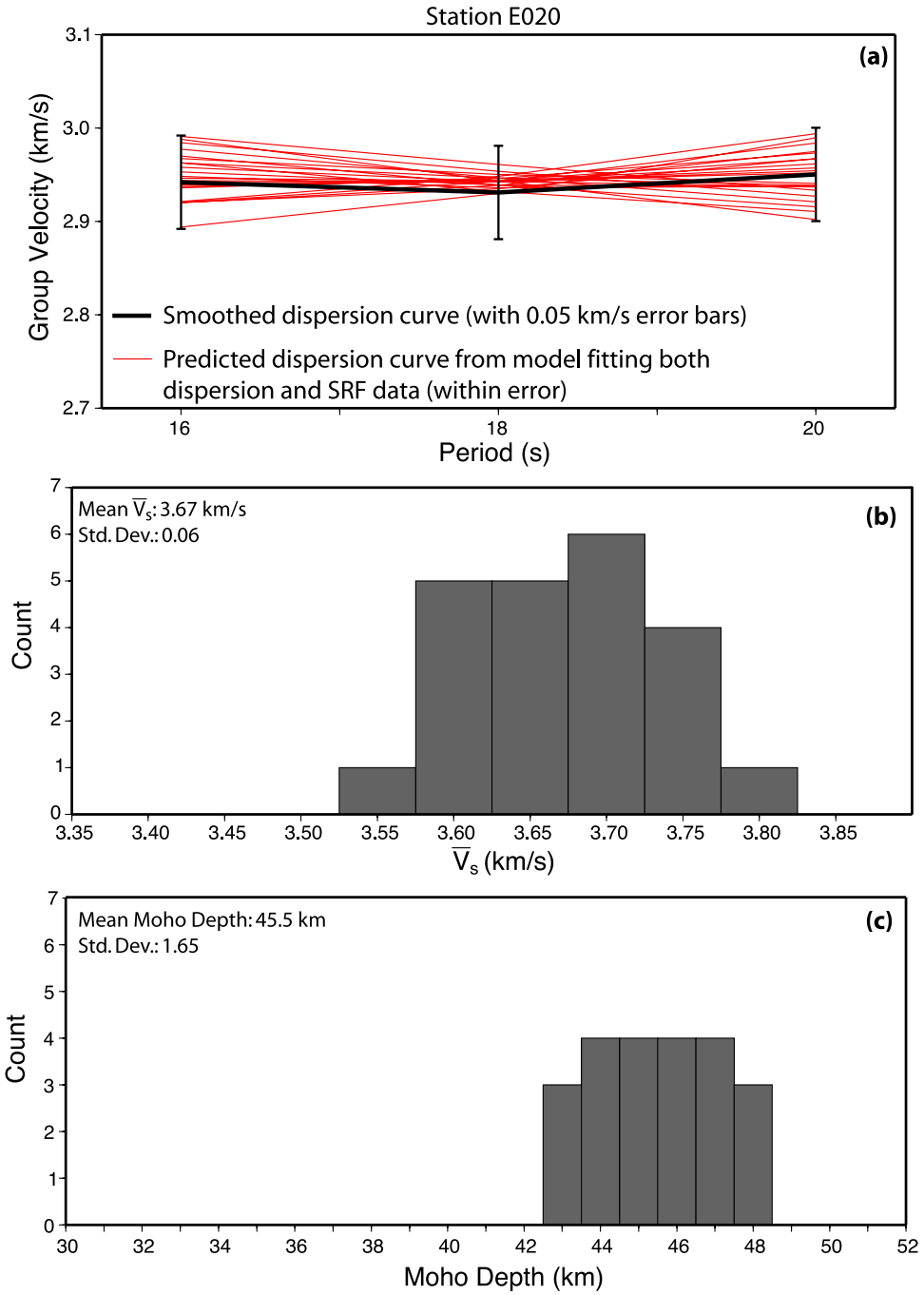

Figure 3. Example of data modeling from ice station E020. (a) Red lines show the predicted group velocity dispersion curves for models that fit the smoothed dispersion data within 0.05 km/s and that fit the SRF Moho Sp time within 0.3 s. In this case, there are 22 "fit" models. (b) The range of $\overline{V}_s$ encompassed by the "fit" models. (c) The range of Moho depths encompassed by the "fit" models. Note that these Moho depths include the thickness of the ice layer.

used to determine an average ray parameter (p). This p was then used to compute the vertical slowness for each layer in the model, which in turn was used to compute the predicted Sp-S time expected for the Moho conversion from that model. To account for variations in the ray parameter between different events contributing to the stack, an uncertainty of 0.3 s was assigned to the observed Moho Sp time. If the predicted Moho Sp time for a given model is within the uncertainty of the ob-

served time, the model is accepted. An example of the data modeling is provided in Figure 3.

2.4. Additional Uncertainty Assessment

[14] The range of models that fit both the smoothed dispersion data and the SRF Moho Sp time within the assigned error provide some estimate of the uncertainty associated with the crustal thickness and $\overline{V}_s$ results. An example of this is shown by the histograms in Figures 3b and 3c. Across all examined stations, the standard deviations associated with the crustal thickness and $\overline{V}_s$ average 1.6 km and 0.06 km/s, respectively.

[15] However, additional uncertainties may also arise from the fixed parameters in the grid search. To assess how much the crustal thickness and $\overline{V}_s$ depend on the values chosen for these parameters, different ranges of ice thickness, ice V_s, and crustal σ were tested. Even for stations underlain by the thickest ice layer, such as station N132 where the ice is ~3.4 km thick, the Sp conversion points at the base of the ice layer are within 1.5 km of the station. Ice-penetrating radar measurements [*Blankenship et al.*, 2001; *Studinger et al.*, 2004] indicate that the ice thickness varies at most by 0.2 km over this distance range. While ice V_s can vary over a fairly wide range depending on the thickness of the firn layer, seismic experiments indicate that the V_s of ice generally falls between about 1.5 and 2.0 km/s [*Kim et al.*, 2007]. Estimates of the crustal σ were obtained from *Finotello et al.* [2008], which fall between 0.24 and 0.27. Maximizing the ice V_s while simultaneously minimizing the ice thickness and crustal σ within the specified limits leads to maximum values of crustal thickness and $\overline{V}_s$. Similarly, minimizing the ice V_s while maximizing the ice thickness and crustal σ leads to minimum crustal parameters. On average, these ranges lead to a 1.5 km uncertainty in Moho depth and a 0.04 km/s uncertainty in $\overline{V}_s$. Combining these uncertainties with those associated with the dispersion data and the SRF Moho Sp times, we estimate that our $\overline{V}_s$ are resolved to within ±0.10 km/s and our Moho depths are resolved to within ±3 km.

2.5. Validating the Grid Search Procedure

[16] To evaluate our modeling approach, our SRF analysis was applied to rock stations E004, E008, and N000, and the $\overline{V}_s$ and Moho depth estimates obtained were compared to those previously determined using PRFs. Beneath stations E004 and E008, our $\overline{V}_s$ is ~3.6 km/s while beneath station N000, it is ~3.5 km/s. Estimates of absolute crustal V_s are somewhat limited in this region, but *Bannister et al.* [2003] estimated crustal V_s between 3.4 and 3.8 km/s beneath nearby station VNDA (Figure 1), which agrees well with our findings. The crustal thicknesses determined by our analysis for stations E004, E008, and N000 are 29, 38, and 33 km, respectively. These estimates agree well with those of *Lawrence et al.* [2006], who used PRFs to obtain crustal thicknesses of 31, 38, and 36 km for the same three stations. Additionally, our results are well matched by those of *Finotello et al.* [2008], who used the H-κ stacking method [*Zhu and Kanamori*, 2000] to examine crustal structure beneath TAMSEIS bedrock stations and reported a ~34 km thick crust beneath station E004 and a ~38 km thick crust beneath stations E008 and N000. The comparable $\overline{V}_s$ and Moho depths determined for the rock stations, whether using PRFs or SRFs, illustrates that our modeling methodology is robust and provides confidence in our results.

3. Results

[17] Our crustal thickness estimates are summarized in Figure 4. Since our analysis produces similar results for rock stations as PRFs, the Moho depth beneath unexamined rock stations was taken from *Finotello et al.* [2008] to extend the profiles to the Ross Sea coastline. Along the EW profile, the Moho depth increases from ~25 km near the coast to ~40 km beneath the TAMs. Moving into EA, there is some indication that the Moho shallows slightly beneath station JNCT; however, it then deepens beneath E018 and E020 to attain a fairly uniform depth of ~44 km beneath the end of the profile (Figure 4a). The $\overline{V}_s$ along the profile averages ~3.6 km/s. Along the NS profile, the Moho depth also increases from the coast inland, changing from ~20 km beneath TNV to ~42 km beneath N036. Along the rest of the profile, the Moho depth across EA is fairly uniform, averaging ~44 km (Figure 4b). $\overline{V}_s$ along this profile ranges from ~3.6 km/s beneath stations in the Wilkes Basin to ~3.7 km/s beneath stations in the Vostok Highlands.

[18] Is it reasonable to interpret the second Sp arrival on the SRFs (Figure 2) as the Sp conversion from the Moho, as we have done? To answer this question, we compare our $\overline{V}_s$ and Moho depth estimates beneath the EA craton to those from other studies of Precambrian crust. Beneath the Archean Yilgarn craton in western Australia, crustal thickness varies from 36 to 46 km, with crustal

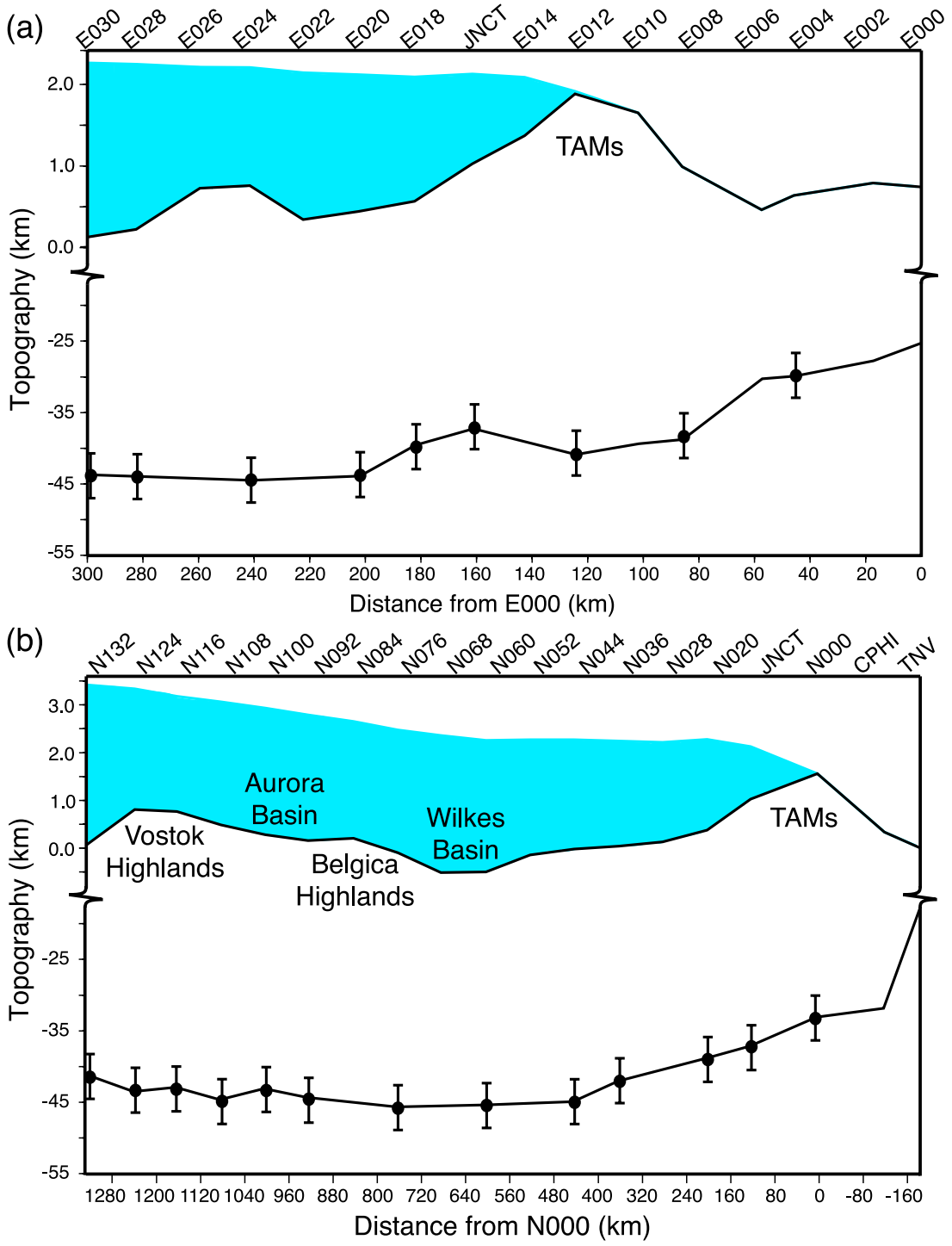

Figure 4. Moho topography along the (a) EW and (b) NS TAMSEIS profiles, in relation to bedrock and surface topography. Note the change of scale on the vertical axis. The blue shaded area indicates ice thickness, and our Moho depth estimates are shown by black dots with ±3 km error bars, as described in the text. Moho depths beneath unexamined rock stations are taken from *Finotello et al.* [2008].

V_s between 3.5 and 3.7 km/s [*Reading et al.*, 2003; *Goleby et al.*, 2004]. In southern Africa, crustal V_s is fairly uniform, ranging from 3.5 to 3.75 km/s, but the crust is thinner (35–40 km) beneath some parts of the Archean Kaapvaal and Zimbabwe cratons and thicker (45–50 km) beneath Proterozoic mobile belts [e.g., *Nguuri et al.*, 2001; *Nair et al.*, 2006]. These trends may also be observed on a

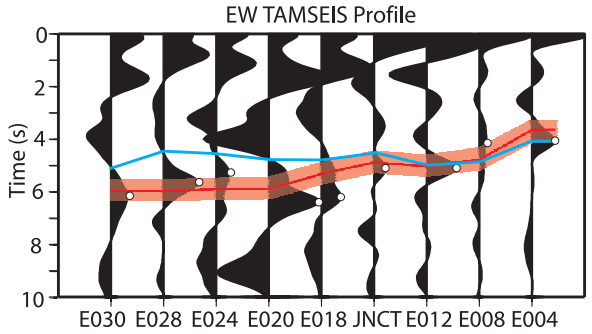

Figure 5. Stacked PRFs along the EW TAMSEIS profile, comparable to Figure 3 of *Lawrence et al.* [2006]. The transition from rock stations to ice stations occurs approximately at station E012. The white circles indicate peaks interpreted as the Moho Ps conversion by *Lawrence et al.* [2006]. The red line denotes the predicted Moho Ps-P arrival time determined using the crustal thickness and velocity estimates from our analysis, with the red shaded area indicating the associated uncertainty. The blue line denotes the predicted Moho Ps-P arrival time determined using the velocity models and crustal thicknesses from *Lawrence et al.* [2006]. Note the mismatch between the blue line and the white circles, especially for the ice stations.

global scale. *Mooney et al.* [1998] compiled 249 measurements of crustal thickness and velocity from Precambrian shields and showed there is little difference in crustal velocity between terrains of different age. They also argued that Archean terrains tend to have somewhat thinner crust (~40 km) compared to Proterozoic ones (~45–47 km). In contrast, *Rudnick and Gao* [2003], who also examined both Archean and Proterozoic terrains, found that crustal thickness ranges from 35 to 43 km regardless of age. The crustal thickness (~44 km) and $\overline{V}_s$ (~3.6 km/s) estimates we obtain for the EA craton are therefore consistent with those found globally for Precambrian terrains, indicating that the second Sp arrival on the SRFs is most likely the Sp conversion from the Moho.

4. Discussion

4.1. Crustal Structure of the EA Craton

[19] Our crustal thickness estimates across the EA craton are ~9 km thicker than those reported by *Lawrence et al.* [2006], who jointly inverted PRFs and Rayleigh wave phase velocities. They obtained a fairly uniform depth of ~35 km for the Moho beneath EA, with an average crustal V_s of ~4 km/s. To investigate this discrepancy, PRFs were generated for stations along the EW TAMSEIS profile, comparable to Figure 3 of *Lawrence et al.* [2006]. For these stations, the Moho depth and crustal velocity estimates from our analysis, along with the associated uncertainties, were used to determine the expected Moho Ps-P arrival time on the corresponding PRF, and these were compared to the Ps conversions interpreted by *Lawrence et al.* [2006, Figure 5]. For several stations, like E018 and E020, our comparison indicates that the Moho Ps arrivals may have been misinterpreted by *Lawrence et al.* [2006], possibly because of the complexity of the PRFs from the ice reverberations. For the remaining stations, there is generally good agreement between the predicted and observed Ps arrival times, illustrating the consistency between the PRFs and SRFs. Therefore, the discrepancy in crustal thickness estimates between our results and those of *Lawrence et al.* [2006] is likely related to differences in velocity. The velocity models and crustal thicknesses presented by *Lawrence et al.* [2006] were also used to determine an expected Moho Ps-P arrival time on the corresponding PRFs. As shown in Figure 5, these predicted times are generally too early, especially for the ice stations, and do not match the observed Ps arrivals well.

4.2. Crustal Structure of the TAMs

[20] Although it is fairly well constrained that uplift of the TAMs began ~55 Ma [*Fitzgerald et al.*, 1986], uncertainties in crustal and upper mantle structure have lead to considerable debate about the origin of the TAMs, and a variety of uplift models have been proposed. For example, *Stern and ten Brink* [1989] and *ten Brink et al.* [1997, and references therein] suggested that the TAMs resulted from broad flexure of the EA lithosphere along its western, rifted edge and that lateral heat conduction from hotter mantle beneath WA provided a thermal load that aided in the uplift. Additionally, they contend that isostatic rebound following erosion of the TAMs also contributed to the uplift. *Studinger et al.* [2004] and *Karner et al.* [2005] suggested that the TAMs developed as the result of rift flank uplift and climate-induced erosional unloading. Their models do not include a thermal anomaly beneath the TAMs but instead require a crustal root beneath the mountain range to provide isostatic buoyancy. Alternatively, *Lawrence et al.* [2006] proposed a hybrid model that includes crustal isostasy, thermal loading, erosional unloading, and a flexural response.

[21] A key constraint to distinguish between competing uplift models is the presence (or lack) of a

crustal root beneath the TAMs. Our results show that the crust beneath station E012 at the crest of the TAMs may be ~3 km thicker than that beneath station JNCT, which is further inland toward the EA craton (Figure 4a). However, along both TAMSEIS profiles, the crust beneath the craton is somewhat thicker than that beneath the TAMs. Therefore, the TAMs are at most underlain by a small root that is locally thicker than the surrounding regions but is thin relative to most of the EA craton. These results differ from those of *Lawrence et al.* [2006] and A. E. Block et al. (Antarctic crustal thickness from satellite gravity: Implications for the Transantarctic and Gamburtsev Subglacial Mountains, submitted to *Earth and Planetary Science Letters*, 2009), who indicate that the crust beneath parts of the TAMs could be ~5 km thicker than the crust beneath parts of EA. Crustal variations along the TAMs front may indicate that the role of thermal versus isostatic buoyancy varies along strike. For the portion of the TAMs examined in the current study, our results do not support uplift models that require a thicker root (≥5 km) beneath the mountain range as a source of buoyancy [*Studinger et al.*, 2004; *Karner et al.*, 2005; *Lawrence et al.*, 2006]. Instead, our findings are more consistent with flexure models, in which the TAMs uplift was driven by thermal loading and erosion [e.g., *ten Brink et al.*, 1997]. Seismic tomography [*Watson et al.*, 2006] and gravity data [*Robinson and Splettstoesser*, 1984; *Stern and ten Brink*, 1989] also suggest similar lithospheric structure beneath EA and the TAMs and corroborate thermally and flexurally driven uplift models for this region of the mountain range.

5. Summary

[22] In this study, we have investigated using SRFs to image the Moho beneath stations deployed on ice using broadband seismic data from two subarrays of the TAMSEIS network. Using standard processing methods, a clear Sp conversion from the Moho can be identified on the SRFs. When combined with Rayleigh wave group velocity measurements, which constrain the average crustal shear velocity, the SRFs lead to crustal thickness estimates with an uncertainty of ≤10%. Across EA, we observe an average crustal thickness of 44 ± 3 km with $\overline{V}_s$ of ~3.6–3.7 km/s, consistent with estimates elsewhere for Precambrian crust. Our results show little evidence for a thick crustal root beneath the examined region of the TAMs; however, given the uncertainty in our Moho depth estimates, a small (2–3 km) crustal root cannot be ruled out.

Acknowledgments

[23] We thank Paul Winberry and the Support Office for Aerogeophysical Research (SOAR) at the University of Texas for providing the ice-penetrating radar data and Marco Finotello for sharing his H-κ stacking results. We also thank Tim Stern and two anonymous reviewers for their thorough critiques of this manuscript. Data were obtained from the IRIS data management center. Funding for this project was provided by National Science Foundation, grants OPP 9909603 and OPP 9909648. Figures 1–5 were prepared using GMT [*Wessel and Smith*, 1998].

References

Bannister, S., J. Yu, B. Leitner, and B. Kennett (2003), Variations in crustal structure across the transition from West to East Antarctica, Southern Victoria Land, *Geophys. J. Int.*, *155*, 870–884, doi:10.1111/j.1365-246X.2003.02094.x.

Blankenship, D., D. Morse, C. Finn, R. Bell, M. Peters, S. Kempf, S. Hodge, M. Studinger, J. Behrendt, and J. Brozena (2001), Geologic controls on the initiation of rapid basal motion for West Antarctic ice streams: A geophysical perspective including new airborne radar sounding and laser altimetry results, in *The West Antarctic Ice Sheet: Behavior and Environment*, *Antarct. Res. Ser.*, vol. 77, edited by R. A. Bindschadler, pp. 105–121, AGU, Washington, D. C.

Farra, V., and L. Vinnik (2000), Upper mantle stratification by P and S receiver functions, *Geophys. J. Int.*, *141*, 699–712, doi:10.1046/j.1365-246x.2000.00118.x.

Finotello, M., J. Julia, A. Nyblade, D. Wiens, and S. Anandakrishnan (2008), Crustal structure along the Transantarctic Mountain Front using receiver functions, *Eos Trans. AGU*, *89*, Fall Meet. Suppl., Abstract T23C-2042.

Fitzgerald, P., M. Sandiford, P. Barret, and J. Gleadow (1986), Asymmetric extension associated with uplift and subsidence in the Transantarctic Mountains and Ross Embayment, *Earth Planet. Sci. Lett.*, *81*, 67–78, doi:10.1016/0012-821X(86)90101-9.

Goleby, B., R. Blewett, R. Korsch, D. Champion, K. Cassidy, L. Jones, P. Groenewald, and P. Henson (2004), Deep seismic reflection profiling in the Archaean northeastern Yilgarn Craton, Western Australia: Implications for crustal architecture and mineral potential, *Tectonophysics*, *388*, 119–133, doi:10.1016/j.tecto.2004.04.032.

Hansen, S., A. Rodgers, S. Schwartz, and A. Al-Amri (2007), Imaging ruptured lithosphere beneath the Red Sea and Arabian Peninsula, *Earth Planet. Sci. Lett.*, *259*, 256–265, doi:10.1016/j.epsl.2007.04.035.

Hansen, S., A. Nyblade, J. Julià, P. Dirks, and R. Durrheim (2009), Upper mantle low velocity zone structure beneath the Kaapvaal Craton from S-wave receiver functions, *Geophys. J. Int.*, *178*, 1021–1027.

Julià, J., R. Herrmann, C. Ammon, and A. Akinci (2004), Evaluation of deep sediment velocity structure in the New Madrid Seismic Zone, *Bull. Seismol. Soc. Am.*, *94*, 334–340, doi:10.1785/0120030081.

Karner, G., M. Studinger, and R. Bell (2005), Gravity anomalies of sedimentary basins and their mechanical implications:

Application to the Ross Sea basins, West Antarctica, *Earth Planet. Sci. Lett.*, *235*, 577–596, doi:10.1016/j.epsl.2005.04.016.

Kim, K., M. Hong, J. Lee, J. Hong, and Y. Jin (2007), Seismic experiments on the Fourcade Glacier in the King George Island, Antarctica, *Geophys. Res. Abstr.*, *9*, A-04755.

Kumar, P., et al. (2005), The lithosphere-asthenosphere boundary in the north-west Atlantic region, *Earth Planet. Sci. Lett.*, *236*, 249–257, doi:10.1016/j.epsl.2005.05.029.

Last, R., A. Nyblade, C. Langston, and T. Owens (1997), Crustal structure of the East African Plateau from receiver functions and Rayleigh wave phase velocities, *J. Geophys. Res.*, *102*, 24,469–24,483, doi:10.1029/97JB02156.

Lawrence, J., D. Wiens, A. Nyblade, S. Anandakrishnan, and D. Voigt (2006), Crust and upper mantle structure of the Transantarctic Mountains and surrounding regions from receiver functions, surface waves, and gravity: Implications for uplift models, *Geochem. Geophys. Geosyst.*, *7*, Q10011, doi:10.1029/2006GC001282.

Li, X., R. Kind, X. Yuan, I. Wolbern, and W. Hanka (2004), Rejuvenation of the lithosphere by the Hawaiian plume, *Nature*, *427*, 827–829, doi:10.1038/nature02349.

Ligorria, J., and C. Ammon (1999), Poisson's ratio variations of the crust beneath North America, *Seismol. Res. Lett.*, *70*, 274.

Lythe, M., D. Vaughan, and B. Consortium (2001), BEDMAP: A new ice thickness and subglacial topographic model of Antarctica, *J. Geophys. Res.*, *106*, 11,335–11,351, doi:10.1029/2000JB900449.

Mooney, W., G. Laske, and T. Masters (1998), CRUST 5.1: A global crustal model at 5° × 5°, *J. Geophys. Res.*, *103*, 727–747, doi:10.1029/97JB02122.

Nair, S., S. Gao, K. Liu, and P. Silver (2006), Southern African crustal evolution and composition: Constraints from receiver function studies, *J. Geophys. Res.*, *111*, B02304, doi:10.1029/2005JB003802.

Nguuri, T., J. Gore, D. James, S. Webb, C. Wright, T. Zengeni, O. Gwavava, J. Snoke, and the Kaapvaal Seismic Group (2001), Crustal structure beneath southern Africa and its implications for the formation and evolution of the Kaapvaal and Zimbabwe cratons, *Geophys. Res. Lett.*, *28*, 2501–2504, doi:10.1029/2000GL012587.

Pyle, M., D. Wiens, A. Nyblade, and S. Anandakrishnan (2008), Ambient noise Rayleigh wave tomography in Antarctica from the TAMSEIS array, *Eos Trans. AGU*, *89*, Fall Meet. Suppl., Abstract S31A-1883.

Reading, A., B. Kennett, and M. Dentith (2003), Seismic structure of the Yilgarn Craton, West Australia, *Aust. J. Earth Sci.*, *50*, 427–438, doi:10.1046/j.1440-0952.2003.01000.x.

Robinson, E., and J. Splettstoesser (1984), Structure of the Transantarctic Mountains determined from geophysical surveys, in *Geology of the Central Transantarctic Mountains*, *Antarct. Res. Ser.*, vol. 36, edited by M. D. Turner and J. F. Splettstoesser, pp. 119–162, AGU, Washington, D. C.

Rudnick, R., and S. Gao (2003), Composition of the continental crust, in *The Crust*, *Treatise on Geochem.*, vol. 3, edited by H. D. Holland and K. K. Turekian, pp. 1–64, Elsevier, Oxford, U. K.

Saito, M. (1988), DISPER80: A subroutine package for calculation of seismic normal-mode solutions, in *Seismological Algorithms: Computational Methods and Computer Programs*, edited by D. J. Doornbos, pp. 293–319, Univ. of Oslo, Oslo.

Stern, T., and U. ten Brink (1989), Flexural uplift of the Transantarctic Mountains, *J. Geophys. Res.*, *94*, 10,315–10,330, doi:10.1029/JB094iB08p10315.

Studinger, M., R. Bell, W. Buck, G. Karner, and D. Blankenship (2004), Subglacial geology inland of the Transantarctic Mountains in light of new aerogeophysical data, *Earth Planet. Sci. Lett.*, *220*, 391–408, doi:10.1016/S0012-821X(04)00066-4.

ten Brink, U., R. Hackney, S. Bannister, T. Stern, and Y. Makovsky (1997), Uplift of the Transantarctic Mountains and the bedrock beneath the East Antarctic ice sheet, *J. Geophys. Res.*, *102*, 27,603–27,621, doi:10.1029/97JB02483.

Watson, T., A. Nyblade, D. Wiens, S. Anandakrishnan, M. Benoit, P. Shore, D. Voigt, and J. VanDecar (2006), P and S velocity structure of the upper mantle beneath the Transantarctic Mountains, East Antarctic craton, and Ross Sea from travel time tomography, *Geochem. Geophys. Geosyst.*, *7*, Q07005, doi:10.1029/2005GC001238.

Wessel, P., and W. Smith (1998), New, improved version of the Generic Mapping Tools released, *Eos Trans. AGU*, *79*, 579, doi:10.1029/98EO00426.

Wilson, D., D. Angus, J. Ni, and S. Grand (2006), Constraints on the interpretation of S-to-P receiver functions, *Geophys. J. Int.*, *165*, 969–980, doi:10.1111/j.1365-246X.2006.02981.x.

Yang, Y., M. Ritzwoller, A. Levshin, and N. Shapiro (2007), Ambient noise Rayleigh wave tomography across Europe, *Geophys. J. Int.*, *168*, 259–274, doi:10.1111/j.1365-246X.2006.03203.x.

Yuan, X., R. Kind, X. Li, and R. Wang (2006), The S receiver functions: Synthetics and data examples, *Geophys. J. Int.*, *165*, 555–564, doi:10.1111/j.1365-246X.2006.02885.x.

Zelt, B., and R. Ellis (1999), Receiver function studies in the Trans-Hudson orogen, Saskatchewan, *Can. J. Earth Sci.*, *36*, 585–603, doi:10.1139/cjes-36-4-585.

Zhu, L., and H. Kanamori (2000), Moho depth variation in Southern California from teleseismic receiver functions, *J. Geophys. Res.*, *105*, 2969–2980, doi:10.1029/1999JB900322.